A SkyMapper view of the Large Magellanic Cloud: the dynamics of stellar populations

Zhen Wan, Magda Guglielmo, Geraint Lewis, Dougal Mackey, Rodrigo A Ibata

▶ **To cite this version:**

Zhen Wan, Magda Guglielmo, Geraint Lewis, Dougal Mackey, Rodrigo A Ibata. A SkyMapper view of the Large Magellanic Cloud: the dynamics of stellar populations. Monthly Notices of the Royal Astronomical Society, 2020, 492 (1), pp.782-795. 10.1093/mnras/stz3493 . hal-03150017

HAL Id: hal-03150017
https://hal.science/hal-03150017v1

Submitted on 22 May 2024

HAL is a multi-disciplinary open access archive for the deposit and dissemination of scientific research documents, whether they are published or not. The documents may come from teaching and research institutions in France or abroad, or from public or private research centers.

L'archive ouverte pluridisciplinaire **HAL**, est destinée au dépôt et à la diffusion de documents scientifiques de niveau recherche, publiés ou non, émanant des établissements d'enseignement et de recherche français ou étrangers, des laboratoires publics ou privés.

Monthly Notices
of the
ROYAL ASTRONOMICAL SOCIETY

MNRAS **492,** 782–795 (2020)
Advance Access publication 2019 December 12

doi:10.1093/mnras/stz3493

A SkyMapper view of the Large Magellanic Cloud: the dynamics of stellar populations

Zhen Wan [1]★ Magda Guglielmo,[1] Geraint F. Lewis [1] Dougal Mackey[2] and Rodrigo A. Ibata[3]

[1]*Sydney Institute for Astronomy, School of Physics A28, The University of Sydney, NSW 2006, Australia*
[2]*Research School of Astronomy and Astrophysics, Australian National University, Canberra, ACT 2611, Australia*
[3]*Observatoire Astronomique, Université de Strasbourg, CNRS, 11, rue de l'Université, F-67000 Strasbourg, France*

Accepted 2019 December 9. Received 2019 October 17; in original form 2019 March 8

ABSTRACT

We present the first SkyMapper stellar population analysis of the Large Magellanic Cloud (hereafter LMC), including the identification of 3578 candidate Carbon Stars through their extremely red $g - r$ colours. Coupled with *Gaia* astrometry, we analyse the distribution and kinematics of this Carbon Star population, finding the LMC to be centred at (RA, Dec.) $= (80.90^\circ \pm 0.29, -68.74^\circ \pm 0.12)$, with a bulk proper motion of $(\mu_\alpha, \mu_\delta) = (1.878 \pm 0.007, 0.293 \pm 0.018)$ mas yr^{-1} and a disc inclination of $i = 25.6^\circ \pm 1.1$ at position angle $\theta = 135.6^\circ \pm 3.3^\circ$. We complement this study with the identification and analysis of additional stellar populations, finding that the dynamical centre for red giant branch stars is similar to that seen for the Carbon Stars, whereas for young stars the dynamical centre is significantly offset from the older populations. This potentially indicates that the young stars were formed as a consequence of a strong tidal interaction, probably with the Small Magellanic Cloud. In terms of internal dynamics, the tangential velocity profile increases linearly within $\sim$3 kpc, after which it maintains an approximately constant value of $V_{\rm rot} = 83.6 \pm 1.7$ km s^{-1} until $\sim$7 kpc. With an asymmetric drift correction, we estimate the mass within 7 kpc to be $M_{\rm LMC}(< 7\,{\rm kpc}) = (2.5 \pm 0.1) \times 10^{10}\,{\rm M}_\odot$ and within the tidal radius ($\sim$30 kpc) to be $M_{\rm LMC}(< 30\,{\rm kpc}) = (1.06 \pm 0.32) \times 10^{11}\ {\rm M}_\odot$, consistent with other recent measurements.

Key words: Magellanic Clouds – galaxies: structure.

1 INTRODUCTION

The Large Magellanic Cloud (LMC) is amongst the largest dwarf galaxies within the Local Volume (see McConnachie 2012), and its complex evolutionary history is encoded in its present structure and dynamics. As such, kinematic observations of the various components of the LMC have revealed the orientation and morphology of its stellar disc (e.g. Freeman, Illingworth & Oemler 1983; Meatheringham et al. 1988; van der Marel et al. 2002; Olsen et al. 2011), with a star formation history which has peaked at several points over the past 5 Gyr (Harris & Zaritsky 2009). Additionally, radio observations of the gaseous components of the LMC, and the more extensive Magellanic System, have revealed the signatures of historical LMC–SMC interactions (e.g. Staveley-Smith et al. 2003; Brüns et al. 2005; Tepper-García et al. 2019), events that are also now known to be encoded in the structure of the peripheral stellar component (Olsen & Salyk 2002; Belokurov et al. 2017; Besla et al. 2016; Mackey et al. 2017; Choi et al. 2018; Nidever et al. 2018; Mackey et al. 2018; Vasiliev 2018). Most recently, Belokurov & Erkal (2019) identified low-surface brightness stellar arms around the LMC from the panoramic view of red giant branch (RGB) stars, further highlighting the results of the LMC–SMC–MW interactions.

The dynamical evolution of the LMC depends upon its mass. For example, Besla et al. (2007, 2010, 2012) proposed that the Magellanic system is currently on its first orbital pass around the Milky Way, requiring a total mass of $M > 10^{11}\,{\rm M}_\odot$ (Kallivayalil et al. 2013). Moreover, recent simulation from Erkal et al. (2019) estimates the LMC mass to be $1.38 \times 10^{11}\ {\rm M}_\odot$ from the perturbation on the Milky Way stellar stream. However, early observational measurements based upon internal kinematics find masses substantially smaller than this; e.g. Meatheringham et al. (1988) estimate a mass of $6 \times 10^9\ {\rm M}_\odot$ from planetary nebulae, whilst Kim et al. (1998) use HI dynamics to estimate the mass of LMC within 4 kpc to be $3.5 \times 10^9\ {\rm M}_\odot$. This low-mass LMC was rejected by van der Marel et al. (2002) with stellar radial velocity measurements, although mass estimates are limted by the paucity of kinematic tracers at large radius.

The dynamical interactions of the Magellanic Clouds can imprint differing signatures on different stellar populations, identifiable in global structure and phase space distributions. For example, the younger stellar population is observed to be more clumpy than older

★ E-mail: zwan3791@uni.sydney.edu.au

© 2019 The Author(s)
Published by Oxford University Press on behalf of the Royal Astronomical Society

Downloaded from https://academic.oup.com/mnras/article/492/1/782/5674120 by guest on 22 May 2024

stars in both LMC and SMC (Small Magellanic Cloud, e.g. Zaritsky et al. 2000; Cioni, Habing & Israel 2000; Nikolaev & Weinberg 2000; Belcheva et al. 2011; Moretti et al. 2014; Mackey et al. 2017), and some carbon-rich AGB (asymptotic giant branch) stars are likely to form a second (or third) disc in the LMC (e.g. Graff et al. 2000; Olsen et al. 2011). We can also see difference in the inclination and position angle estimations of the different disc populations (e.g. Kim et al. 1998; van der Marel 2001; Haschke, Grebel & Duffau 2012; Subramanian & Subramaniam 2013; Deb & Singh 2014; Subramanian & Subramaniam 2015; Jacyszyn-Dobrzeniecka et al. 2016; Inno et al. 2016). By comparing different population, hence we can infer the history of the LMC.

The current SkyMapper (Wolf et al. 2018) and *Gaia* (Gaia Collaboration et al. 2018) surveys provide a means of identifying different populations, especially Carbon Stars in the Magellanic Clouds, with essentially minimal contamination, thus facilitating a detailed kinematic portrait of the LMC and enabling comparisons of different populations within same context. As detailed in the following sections, the SkyMapper photometric system is ideally suited to identifying the Carbon Star population of the LMC; as luminous intermediate-age stars distinguishable by their broad carbon absorption, they represent excellent tracers of the structure and kinematics of the LMC. For instance, Carbon Stars have been used to measure the configuration of LMC (e.g. van der Marel et al. 2002) with catalogues from Kunkel, Irwin & Demers (1997) and Hardy et al. (2001).

In this contribution, we present the first results of our stellar population survey of the LMC, using the derived kinematics to determine its mass and compare the dynamical signatures of differing populations. In Section 2, we discuss the selection of different populations from the SkyMapper derived colour–magnitude diagram (CMD) and describe their basic properties. In Section 3, we examine the derived kinematic profile using our Carbon Star sample and estimate the mass of the LMC. Additionally, we further present complementary analyses for young and RGB stars. We conclude the paper in Section 4.

2 DATA

The aim of SkyMapper is to create a deep, multi-epoch, multicolour digital survey of the entire southern sky (Wolf et al. 2018). The first all-sky data release of SkyMapper (DR1) covers 20 200 deg^2 of the sky, with almost 300 million detected stellar and non-stellar sources.

The CMD of stars in the Magellanic Clouds region within 10° of (RA, Dec.) = (81°.91, −69°.87), the LMC centre from van der Marel et al. (2002), is obtained from the slightly updated SkyMapper DR1.1 with the following photometric quality selections:

$$\begin{aligned} \mathrm{nimaflags} &= 0, \\ \mathrm{flags} &= 0, \\ \mathrm{ngood} &> 1, \\ \mathrm{ngood\_}min &> 1 \text{ and} \\ nch\_max &= 1 \end{aligned} \quad (1)$$

Fig. 1 shows the resultant CMD, noting that we have excluded some foreground stars based on their *Gaia* parallax (see below).[1] A number of features appear in the CMD, with hot young stars dominating at bluer colours, whilst RGB stars dominate in the red. In addition, there is a prominent sequence of extremely red stars with $(g-r)_0 > 1.2$ mag, and $g_0 \approx 17$ mag; this we identify as Carbon Star candidates in the LMC. Fig. 2 presents the total sample of stars with $(g-r)_0 > 1.2$ mag from SkyMapper; this map reveals that the main concentrations other than in the Galactic plane are Carbon Stars in the LMC and SMC (orange points).

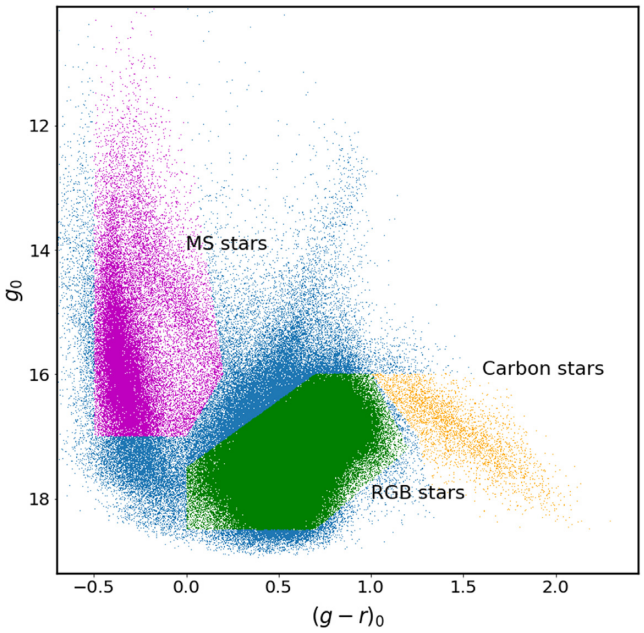

Figure 1. The SkyMapper $(g-r)_0$ versus g_0 CMD of stars within 10° of (R.A., Dec.) = (81°.91, −69°.87). Foreground stars with parallax measurements $\varpi > 0.1$ are excluded to reduce contamination. Young MS stars are dominant between $-1 < (g-r)_0 < 0$ (selected as the magenta region), and older evolved stars (RGB) are in $0 < (g-r)_0 < 1$ (green selected region). The reddest branch (orange points) is the Carbon Star population.

We confirm the Magellanic Carbon Star candidates through two approaches. First, we take stellar spectra from 'The X-Shooter Spectral Library' (Chen et al. 2014) and integrate over the SkyMapper filter transmission curves (Bessell et al. 2011), to obtain the expected SkyMapper colour for different stellar types. In Fig. 3, we find Carbon Stars from this spectral library, marked as 'C', are closely aligned with the candidate LMC and SMC Carbon Stars from SkyMapper. Secondly, we cross-matched all SkyMapper stars in the LMC region with the LMC Carbon Star catalogue of Kontizas et al. (2001). Fig. 4 presents the CMD of the matched Carbon Stars. Comparing their catalogue to our selected Carbon Star sample, we find excellent consistency between the two groups. Most Carbon Stars have SkyMapper colour $(g-r)_0 > 1$ mag and if we assume that the distance modulus of the LMC is 18.5 mag, the typical absolute magnitude is $M_g \approx -1$ mag.

We selected 3578 candidate LMC Carbon Stars from SkyMapper in total. These stars extend up to ≈ 9 kpc from the LMC centre (see Section 3 and Fig. 8). Although these are rare objects, their high luminosity, and the fact that a simple colour-cut essentially remove all Galactic contamination, together means that they constitute an excellent sample for tracing the dynamical properties of the LMC.

Since the LMC is a highly complex galaxy with a very extended star formation history, we also consider RGB stars (selected using the green region in Fig. 1) and upper main-sequence (MS) stars (selected from the magenta region in Fig. 1) as complementary

[1]The SkyMapper photometric data have been de-reddened using the Schlegel, Finkbeiner & Davis (1998) extinction map with the correction by Schlafly & Finkbeiner (2011).

Downloaded from https://academic.oup.com/mnras/article/492/1/782/5674120 by guest on 22 May 2024

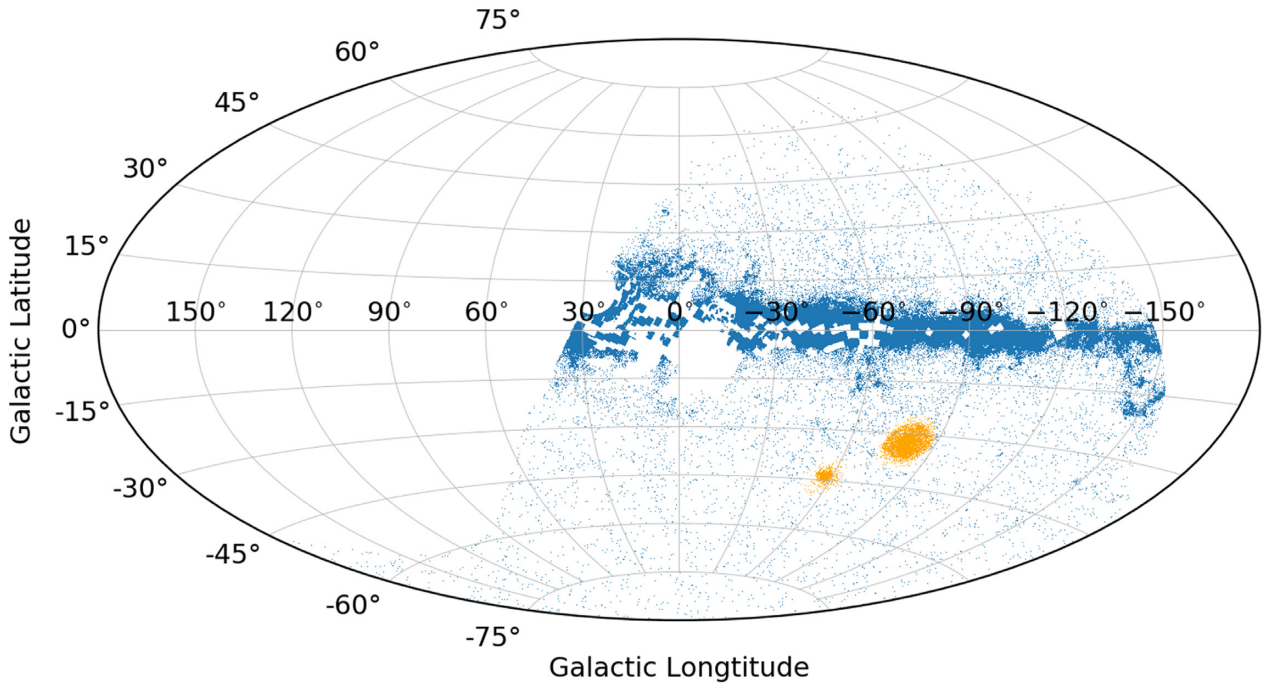

Figure 2. The distribution of stars with $(g - r)_0 > 1.2$ from SkyMapper, with stars concentrated in the Galactic disc and Magellanic Clouds. The orange points denote the concentration of Carbon Star candidates within 10° of (RA, Dec.) = (81°.91, −69°.87), the LMC centre from van der Marel et al. (2002), and within 4° of (RA, Dec.) = (16°.25, −72°.42), the SMC centre from Stanimirović, Staveley-Smith & Jones (2004).

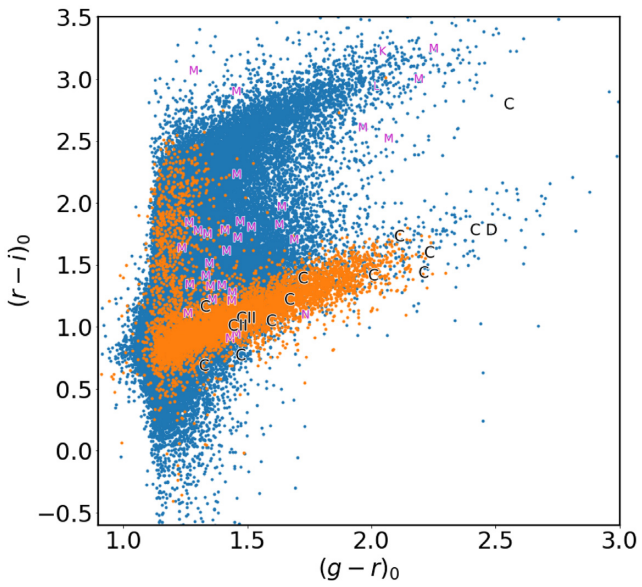

Figure 3. The colour–colour diagram of stars with $(g - r)_0 > 1$ from SkyMapper. Orange points correspond to the stars in Magellanic Clouds region. Blue points are from other regions excluding the Magellanic Clouds. The text in this figure marks the spectral type and indicates the location in the two-colour plane of stars of different spectral types derived using spectra from the X-Shooter Spectral Library integrated over the SkyMapper transmission curves (Section 2). Spectra marked with 'C' indicate Carbon Stars from this library.

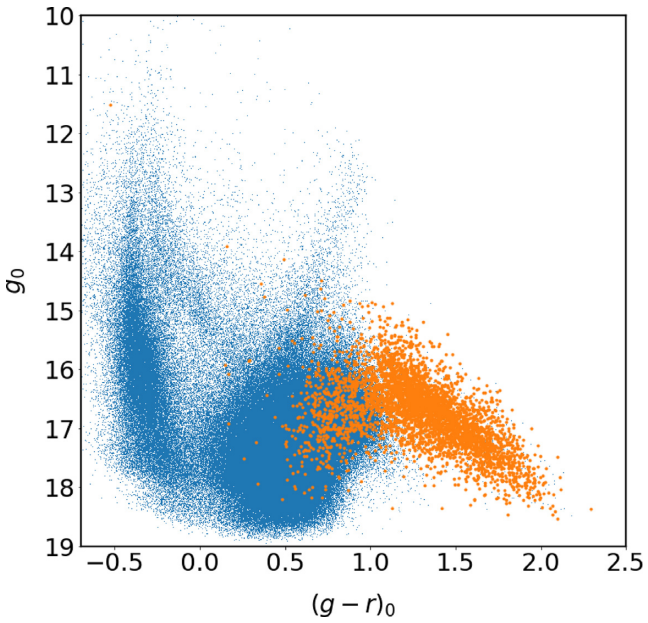

Figure 4. The SkyMapper CMD of Carbon Stars from Kontizas et al. (2001, orange points). We find a good match between their catalogue and our Carbon Star sample. This demonstrates that the Carbon Stars are, in general, well separated from RGB stars in the SkyMapper g and r bands, providing an effective way to identify and isolate these stars.

tracers of ancient and young stellar populations, respectively. While the Carbon Stars constitute the primary data set for our analysis, these additional samples allow us to explore variations in the dynamical properties of stellar populations in the LMC.

We cross-match each of the three samples (Carbon Stars, RGB stars, and upper MS stars) with *Gaia* DR2 (Gaia Collaboration et al. 2016, 2018) to obtain astrometric information. The data quality of the current release (DR2) is insufficient to detect parallax precisely at the distance of the LMC, and hence we removed any sources with

Downloaded from https://academic.oup.com/mnras/article/492/1/782/5674120 by guest on 22 May 2024

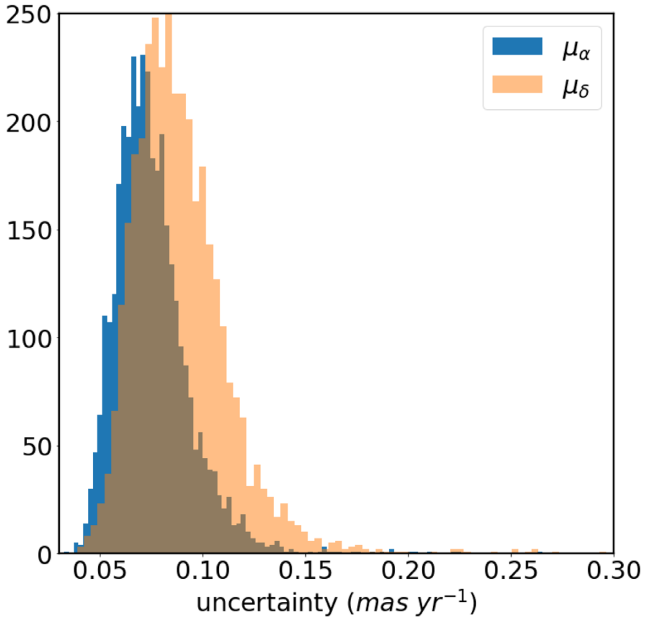

Figure 5. The uncertainty in *Gaia* DR2 proper motion for the selected Carbon Star candidates, with a typical uncertainty of $\sim$0.07 mas yr^{-1}.

parallaxes inconsistent with zero at 3σ as foreground contaminants (cf. Fig. 1).

In Fig. 5, we present the distribution of measurement uncertainties in the two proper motion components for our Carbon Star sample. The typical uncertainty for these stars in *Gaia* DR2 is $\sim$0.07 mas yr^{-1}. At the distance of the LMC, this uncertainty roughly corresponds to $\sim$16.5 km s^{-1}.

3 RESULTS

3.1 Kinematics

The observed proper motions of the stars in LMC consist of the bulk motion and their internal motion relative to the LMC system. Because the LMC has a large angular size, variations in viewing perspective mean that the apparent contribution due to the bulk motion changes as a function of position on the sky. Therefore, we model the motions of the stellar sample as:

$$\boldsymbol{V} = \boldsymbol{V}_{\rm bulk} + \boldsymbol{V}_{\rm inter} \tag{2}$$

Here, $\boldsymbol{V}$ is the 3D velocity, while $\boldsymbol{V}_{\rm inter}$ describes the internal velocities and $\boldsymbol{V}_{\rm bulk}$ is the bulk motion of the LMC. The latter has two components in proper motion that we set as free parameters, and one line-of-sight component that we fix as 262.2 km s^{-1}(van der Marel et al. 2002). In modelling the internal velocity components, we assume a simplified model where the Carbon Stars are in a thin rotating disc where the x, y, z coordinate system centred at the LMC centre and the disc lies on the xy-plane. The rotation curve is given by:

$$\begin{aligned} V_\phi &= \omega\, r, \ \text{for}\ r < r_0 \\ V_\phi &= \omega\, r_0, \ \text{for}\ r \geq r_0 \end{aligned} \tag{3}$$

where $r = \sqrt{x^2 + y^2}$ is the deprojected in-plane radius; r_0 is the break radius; ω is the constant angular speed of the inner regions of the LMC; ϕ is the in-plane directional angle; and V_ϕ is the rotational speed. In this simple model, we assume no net velocity components in the z- and r-directions, and consider a constant in-plane radial ($\sigma_{\rm r}$) and a tangential velocity dispersion (σ_ϕ).

We then project the total velocity into the sky by assuming that the LMC disc is in a plane tilted with respect to the line of sight. The dynamical centre, denoted as α_0 and δ_0, are set as free parameters, with the distance to the LMC centre assumed to be 49.9 kpc (de Grijs, Wicker & Bono 2014). To define the 3D velocity, we need two additional quantities: the position angle θ (from north to east as suggested in van der Marel et al. 2002) of the line of nodes and the inclination angle i. These are free parameters in our model. We define our transformations as:

$$\begin{aligned} \boldsymbol{V}_{\rm sky} &= \mathbb{R}_{\rm x}(i) \cdot \mathbb{R}_z(\theta - \pi) \cdot \mathbb{R}_{\rm x}\left(\delta_0 - \frac{\pi}{2}\right) \cdot \mathbb{R}_z\left(\alpha_0 - \frac{\pi}{2}\right) \cdot \boldsymbol{V} \\ \mu_\alpha &= -V_{\rm sky}(x)\sin(\alpha) + V_{\rm sky}(y)\cos(\alpha) \\ \mu_\delta &= V_{\rm sky}(z)\cos(\delta) - (V_{\rm sky}(x)\cos(\alpha) + V_{\rm sky}(y)\sin(\alpha))\sin(\delta) \end{aligned} \tag{4}$$

where $\mathbb{R}$ is the rotation matrix along the corresponding axis, α and δ is the sky position of each Carbon Star in the sample, and $V_{\rm sky}(x)$ is the component of $\boldsymbol{V}_{\rm sky}$ in Cartesian coordinates. This model builds up a correlation between in-plane velocity and proper motion of stars as a function of star position.[2] We explore the likelihood space with an Markov chain Monte Carlo (MCMC) sampling algorithm (Foreman-Mackey et al. 2013) to find the best-fitting model and corresponding uncertainties on parameters. Fig. 6 shows the corner plot summary of the MCMC sampling results. The best parameter values are:

$$\begin{aligned} \alpha_0 &= 80.90^\circ \pm 0.29, & \delta_0 &= -68.74^\circ \pm 0.12 \\ \mu_\alpha &= 1.878 \pm 0.007\ \text{mas yr}^{-1}, & \mu_\delta &= 0.293 \pm 0.018\ \text{mas yr}^{-1} \\ \theta &= 135.6^\circ \pm 3.3, & i &= 25.6^\circ \pm 1.1 \\ \omega &= 24.6 \pm 0.6\ \text{km s}^{-1}\ \text{kpc}^{-1}, & r_0 &= 3.39 \pm 0.12\ \text{kpc} \\ \sigma_r &= 0.157 \pm 0.003\ \text{mas yr}^{-1}, & \sigma_\phi &= 0.158 \pm 0.003\ \text{mas yr}^{-1} \end{aligned} \tag{5}$$

We summarize the LMC parameters from our best-fitting configuration model and compare them to literature values in Table 1. Here, we also list the fitting results from the RGB stars and MS stars; see the detailed discussion on Section 3.4

The bulk motions from the differing measurements are in general agreement. We note that the inferred bulk proper motions are correlated with the assumed dynamical centre (cf. Fig. 6). This means that an identical intrinsic true-space motion will result in a varied measurement of the proper motion, if the reference centre under consideration is different. This is the main cause of the difference between each results. For example, as Helmi et al. (2018) suggest, if the dynamical centre were fixed as the photometric centre from van der Marel (2001), then the their proper motion would be (1.890, 0.314) mas yr^{-1}. For Carbon Stars, the best-fitting configuration parameter θ agrees well with other works listed in the table, and i agrees closely with the purely geometric measurement from Inno et al. (2016) and Choi et al. (2018).

In the following analysis, unless specified otherwise, the bulk motion has been subtracted from all velocities using our best-fitting proper motion results and the assumed line-of-sight velocity. In the left-hand panel of Fig. 7, we see that the residual proper motions for the Carbon Stars indicate they are clearly rotating around the LMC centre. Also shown in this panel, our inferred dynamical centre for

[2]See Appendix A for details of the correlation and the corresponding Jacobian matrix and determinant.

Downloaded from https://academic.oup.com/mnras/article/492/1/782/5674120 by guest on 22 May 2024

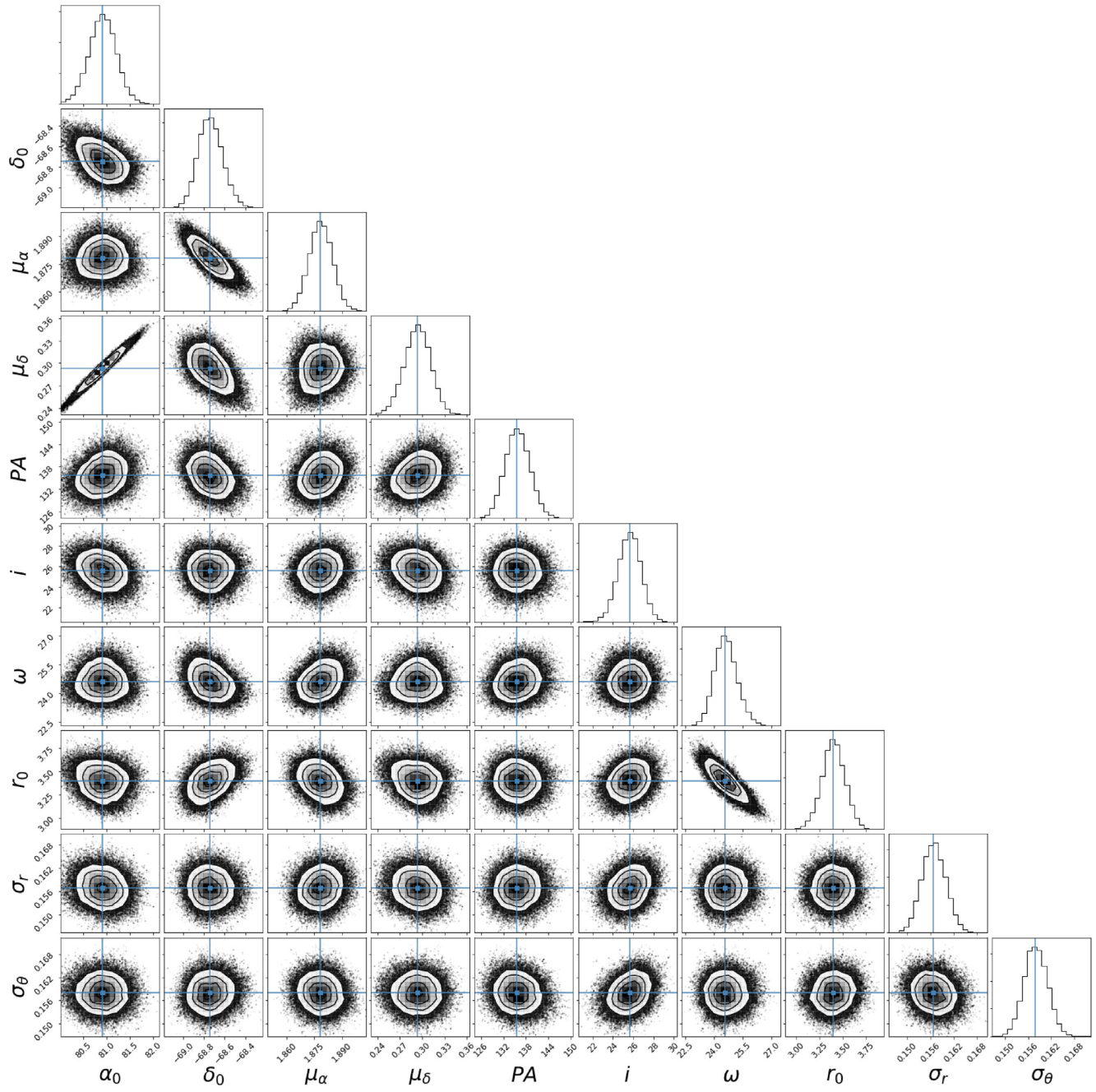

Figure 6. Corner plot summary of the MCMC sampling result for the Carbon Stars. A significant correlation is evident between the inferred proper motion and the inferred dynamical centre of the LMC. Additionally, the parameters ω and r_0 are correlated, as $\omega \times r_0$ represents the flat rotation velocity. This figure (as well as Figs B1 and B2) is made with the *corner* package (Foreman-Mackey et al. 2016).

the Carbon Star sample differs from the HI dynamical centre, and the photometric centre of the LMC.

In the right-hand panel of Fig. 7, we show the distribution of proper motions for our Carbon Stars compared to those for the RGB sample (selected from the SkyMapper CMD as shown in Fig. 1). The bar clearly stands out in the map of RGB stars with higher proper motion, whereas this is not clear in the Carbon Star distribution, suggesting that the Carbon Stars are generally not drawn from the bar. Interestingly, Olsen et al. (2011) suggest that part of the Carbon-rich AGB stars are likely to be counter-rotating or form a second disc that have different inclination. They also found those stars have a distribution that avoids the LMC bar.

Fig. 8 shows the tangential (top) and radial (bottom) velocity profile. In both panels, the grey shaded region represents the best-fitting model, and the widths of the grey region represent the dispersions. As inferred in the top panel of this figure, the rotation speed gradually increases inside ~ 3 kpc, in agreement with the results of Helmi et al. (2018). After this point, the rotation speed flattens to $V_{\rm rot} = 83.6 \pm 1.7\,{\rm km\,s^{-1}}$, corresponding to a proper motion of $\sim 0.353\,{\rm mas\,yr^{-1}}$. The average tangential speed may

Downloaded from https://academic.oup.com/mnras/article/492/1/782/5674120 by guest on 22 May 2024

Table 1. The LMC reference or fitted parameters from our best-fitting model and from the literature. The first column is the centre point; the second column is the corresponding bulk motion of the LMC; the third column is the position angle of the line of nodes; and the fourth column is the inclination angle.

Dynamical centre	Bulk motion ($\mu_{\alpha*}$, μ_δ) (mas yr^{-1})	θ (°)	i (°)	Reference
$(80.90 \pm 0.29, -68.74 \pm 0.12)^a$	$(1.878 \pm 0.007, 0.293 \pm 0.018)^a$	$(135.6 \pm 3.3)^a$	$(25.6 \pm 1.1)^a$	Carbon Stars in this work
$(81.23 \pm 0.04, -69.00 \pm 0.02)$	$(1.824 \pm 0.001, 0.355 \pm 0.002)$	(134.1 ± 0.4)	(26.1 ± 0.1)	RGB Stars in this work
$(80.98 \pm 0.07, -69.69 \pm 0.02)$	$(1.860 \pm 0.002, 0.359 \pm 0.004)$	(152.0 ± 1.0)	(29.4 ± 0.4)	Young MS in this work
$(81.91 \pm 0.98, -69.87 \pm 0.41)$	–	129.9 ± 6.0	34.7 ± 6.2^b	van der Marel et al. (2002)
$(81.91 \pm 0.98, -69.87 \pm 0.41)^c$	–	142 ± 5	34.7 ± 6.2^b	Olsen et al. (2011)
$(78.76 \pm 0.52, -69.19 \pm 0.25)$	$(1.910 \pm 0.020, 0.229 \pm 0.047)$	147.4 ± 10.0	39.6 ± 4.5	van der Marel & Kallivayalil (2014)
$(80.78, -69.30)^e$	–	150.76 ± 0.07	25.05 ± 0.55	Inno et al. (2016)
$(78.77, -69.01)^d$	$(1.850 \pm 0.030, 0.234 \pm 0.030)$	$[106.4, 134.6]^f$	[30.1, 61.5]	Helmi et al. (2018)
$(82.25, -69.5)^b$	–	$149.23^{+6.43}_{-8.35}$	$25.86^{+0.73}_{-1.39}$	Choi et al. (2018)
$(81, -69.75)$	–	[130, 135]	[32, 35]	Vasiliev (2018)

[a]The uncertainties are from MCMC sampling. [b]Taken from van der Marel (2001). [c]Taken from van der Marel et al. (2002). [d]Taken from HI centre (Luks & Rohlfs 1992). [e]Cepheids centroid in Inno et al. (2016). [f]See Helmi et al. (2018) for a detailed model discussion

exhibit a mild decrease at large radii (beyond ∼7 kpc), although this conclusion is only tentative due to the paucity of data in this region. The bottom panel in Fig. 8 shows that the radial speed averages to approximately zero, with a slightly increasing tendency outwards.

3.2 Mass

The total LMC mass is known to be a key factor for the first-infall scenario, where a massive LMC ($> 1 \times 10^{11}$ M$_\odot$) is required to ensure that the Clouds evolved as a bound pair for at least 5 Gyr to form the Magellanic Stream (Besla et al. 2012). As shown in Kallivayalil et al. (2013), the first-infall scenario becomes more likely for massive LMC; a massive LMC moreover implies a relatively rapid merger with the Milky Way ∼2.5 Gyr from now (Cautun et al. 2019).

Whilst the LMC is thought to possess a massive dark matter halo, a lack of dynamical tracers at very large radii has limited the determination of the total LMC mass through kinematic means. Instead, the total mass is generally inferred through more indirect methods. For instances, Peñarrubia et al. (2016), considering the timing argument within the Local Group, proposed an infall LMC mass equal to $(2.5 \pm 0.9) \times 10^{11}$ M$_\odot$; Cautun et al. (2019) showed that in the EAGLE[3] cosmological simulations, LMC-mass satellites with an SMC-like companion typically have a total halo mass of $(3.0^{+0.7}_{-0.8}) \times 10^{11}$ M$_\odot$. Erkal et al. (2019) inferred the total LMC mass to be $(1.38^{+0.27}_{-0.24}) \times 10^{11}$ M$_\odot$ from the observed perturbation on the Orphan stellar stream in the Milky Way halo; Erkal & Belokurov (2019) estimated a lower limit of 1.24×10^{11} M$_\odot$ in order to bind the six most-likely infalling dwarf companions of the Magellanic system, and Belokurov & Erkal (2019) showed that simulations with a low LMC mass (2×10^{10} M$_\odot$) can better explain the observed northern spiral structure of the LMC, partly as a consequence of the recent interaction with the Milky Way.

From our best-fitting model, we estimate the LMC mass by considering the circular velocity and adopting the approach discussed in van der Marel et al. (2002): $V^2_{\rm circ} = V^2_{\rm rot} + \kappa\sigma^2_{\rm rad}$, where $\kappa = 6$ and $\sigma_{\rm rad}$ is the dispersion of the radial velocity profile, which together constitute the *asymmetric drift* correction. Noting that our best-fitting values of $V_{\rm rot} = 83.6 \pm 1.7$ km s^{-1}, and the radial dispersion $\sigma_{\rm rad} = 0.157 \pm 0.003$ mas yr^{-1}, corresponding to 37.1 km s^{-1}, we obtain a circular velocity equal to $V_{\rm circ} \sim 123.6 \pm 1.9$ km s^{-1} at 7 kpc. Using the equation $M = V^2_{\rm circ} r/G$ and $G = 4.3007 \times 10^{-6}$ kpc (km s^{-1})^2 M$_\odot^{-1}$, we estimate an upper limit on LMC mass within 7 kpc to be $M_{\rm LMC}(< 7\,{\rm kpc}) = (2.5 \pm 0.1) \times 10^{10}$ M$_\odot$. This mass agrees with other estimations based on stellar dynamics, e.g. van der Marel & Kallivayalil (2014) and van der Marel et al. (2002). van der Marel & Kallivayalil (2014) estimated the tidal radius to be 22.3 ± 5.2 kpc, whilst Navarrete et al. (2019) found stars that match the expected velocity gradient for the LMC halo extending up to 29 kpc away from the LMC centre. If we assume that the circular velocity remains constant out to 30 kpc, the mass within tidal radius is $(1.06 \pm 0.32) \times 10^{11}$ M$_\odot$.

Whilst we note the lack of data at large radii, both the velocity dispersion and the tangential velocity tentatively exhibit a decreasing tendency with radius in Fig. 8 (see also the dispersion profile in Vasiliev 2018). If true, this would imply that our total extrapolated mass within an assumed tidal radius of 30 kpc is likely to be an upper limit. However, determining the tidal radius is difficult, so the total mass would be an approximate estimation. In the future – potentially during *Gaia* DR3 era – the tidal radius can be more accurately determined, yielding a better dynamical mass estimation. Generally, this result matches recent mass estimations from e.g. van der Marel & Kallivayalil (2014), Erkal et al. (2019), and Erkal & Belokurov (2019), while smaller than (or at the lower end of) the LMC mass from e.g. Peñarrubia et al. (2016), Cautun et al. (2019), Shao et al. (2018), and Garavito-Camargo et al. (2019). As previously noted, the mass of the LMC is crucial for understanding its evolutionary history. Not only does the first infall scenario require the LMC to be larger than $\sim 1 \times 10^{11}$ M$_\odot$ (Kallivayalil et al. 2013), a lower mass LMC also leads to a much later LMC–MW merger (Cautun et al. 2019) and produces substantially less perturbation in the Milky Way halo during its infall (Garavito-Camargo et al. 2019).

3.3 Velocity dispersions

As noted above, and described in detail in the Appendix, our model for the velocity properties of the Carbon Star sample in the LMC also incorporates the velocity dispersion in the rotational and radial directions, found to be $(\sigma_{\rm r}, \sigma_\theta) = (0.157 \pm 0.003,\ 0.158 \pm 0.003)$ mas yr^{-1} corresponding to ∼37 km s^{-1} (Fig. 8), which is comparable with the dispersion in the inner LMC derived from Vasiliev (2018). This dispersion significantly contributes to the total mass estimate via the *asymmetric-drift* correction (e.g. van der Marel et al. 2002; Dehnen & Binney 1998, and our estimation in Section 3.2).

[3]Evolution and Assembly of GaLaxies and their Environments

Downloaded from https://academic.oup.com/mnras/article/492/1/782/5674120 by guest on 22 May 2024

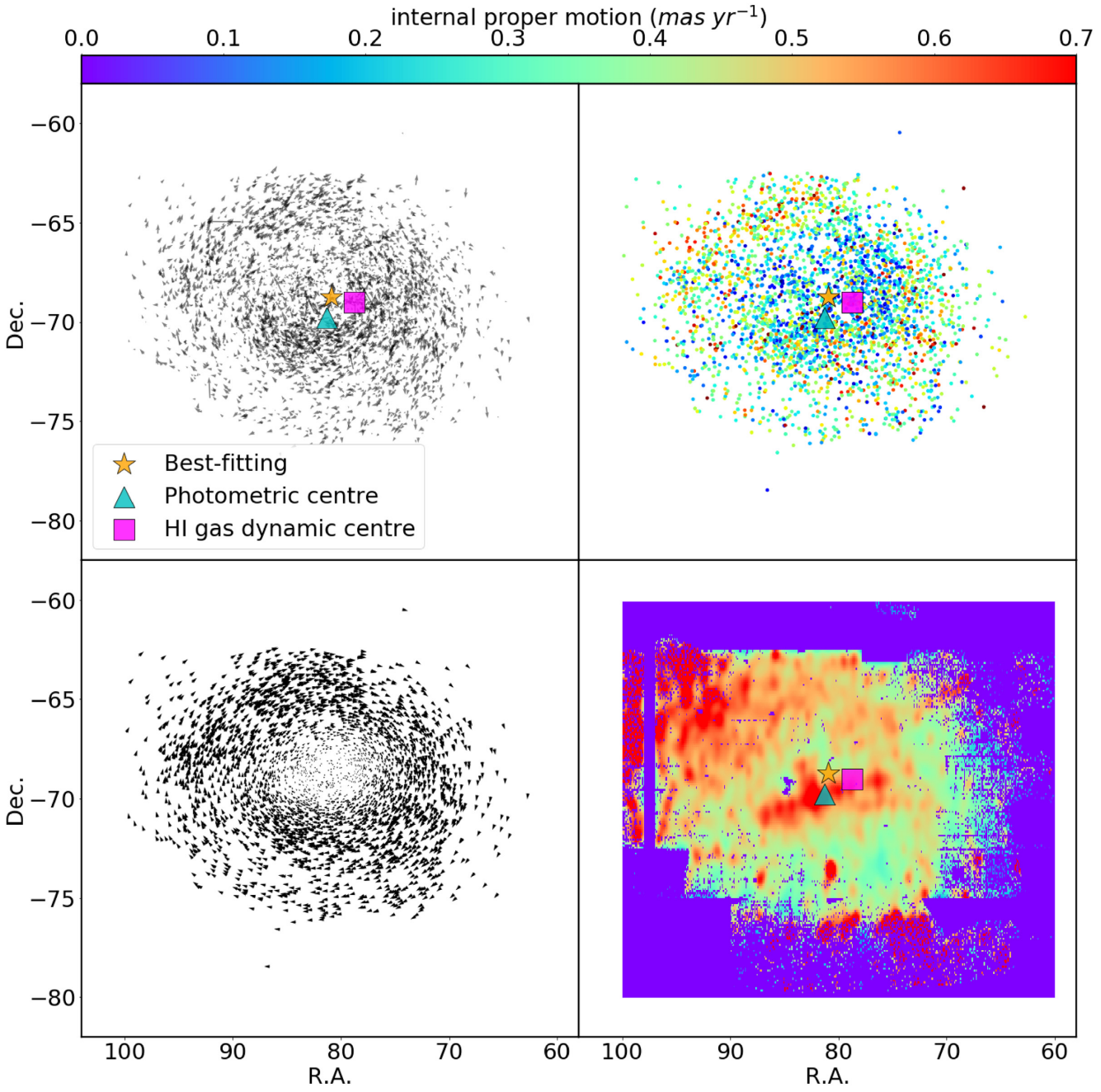

Figure 7. Left, top: the proper motion of Carbon Star candidates with the bulk proper motion of the LMC subtracted, clearly demonstrating rotation around the LMC centre. We mark our best-fitting centre, the photometric centre, and the HI dynamical centre with the symbols noted. Clearly the best-fitting stellar dynamical centre is offset from both the photometric centre (van der Marel 2001) and the HI dynamical centre (Luks & Rohlfs 1992). Bottom: the proper motion from our model. The model qualitatively matches the observed rotation, though the dispersion also present in the observational data is not reproduced in this panel. Right: the distribution of Carbon Stars (top), colour coded with their proper motion, and the proper motion heat map of RGB stars (bottom) with pixel size equal to $1^\circ \times 1^\circ$, which has been smoothed with a Gaussian kernel of 3 pixels in size. In the RGB star heat map, the stellar bar clearly stands out with high proper motion at the LMC photometric centre. However, the Carbon Stars show no significant similar feature. This comparison indicates that the Carbon Stars are more likely to be located in the disc rather than the bar of the LMC.

It is possible that dynamical interactions between the LMC and SMC, the most recent of which likely occurred $\sim 100 - 200$ Myr ago, have had a substantial effect on the velocity dispersion in the LMC. Interactions between the LMC and SMC are supported by several lines of evidence. For example, in the SMC, the gas outflow found by McClure-Griffiths et al. (2018) and the shell of young stars recently studied by Martinez-Delgado et al. (2019) are both indicative of possible interactions with the LMC. For the LMC, Choi et al. (2018) recently identified an outer warp in the disc, and a tilted bar, using red clump stars, consistent with a close encounter with the SMC (see also, Besla et al. 2012; Noël et al. 2013; Guglielmo et al. 2014; Carrera et al. 2017;

Downloaded from https://academic.oup.com/mnras/article/492/1/782/5674120 by guest on 22 May 2024

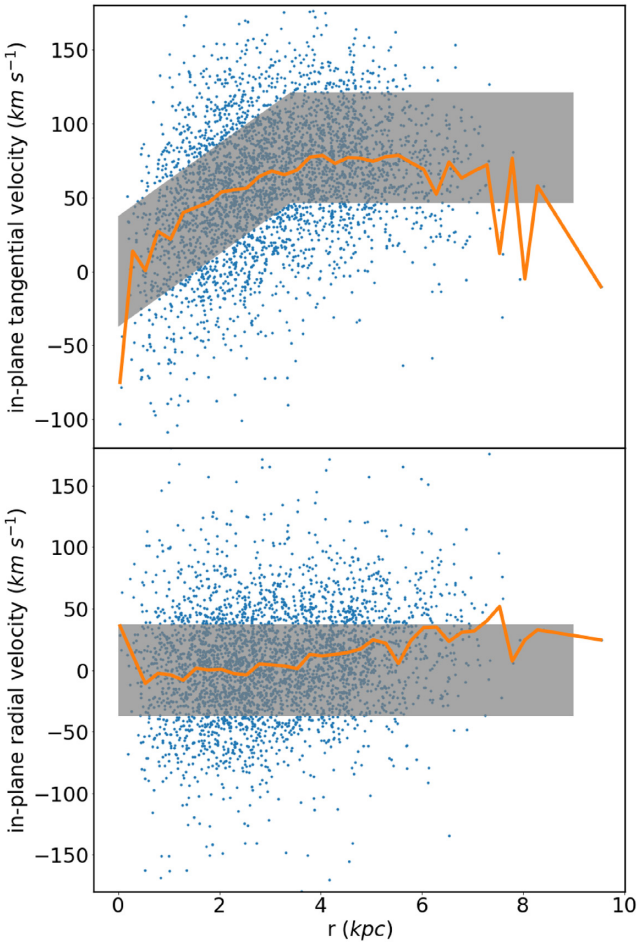

Figure 8. The rotational (top) and radial (bottom) speed profiles as a function of radius for Carbon Stars and the best-fitting kinematic model, indicating an asymptotic flat rotation speed of $V_{\rm rot} = 83.6 \pm 1.7\,{\rm km\,s^{-1}}$. The radial speed is scattered around 0, with the grey shading indicating the best-fitting dispersion as a function of radius. The orange lines indicate the average velocity within 0.25 kpc bins.

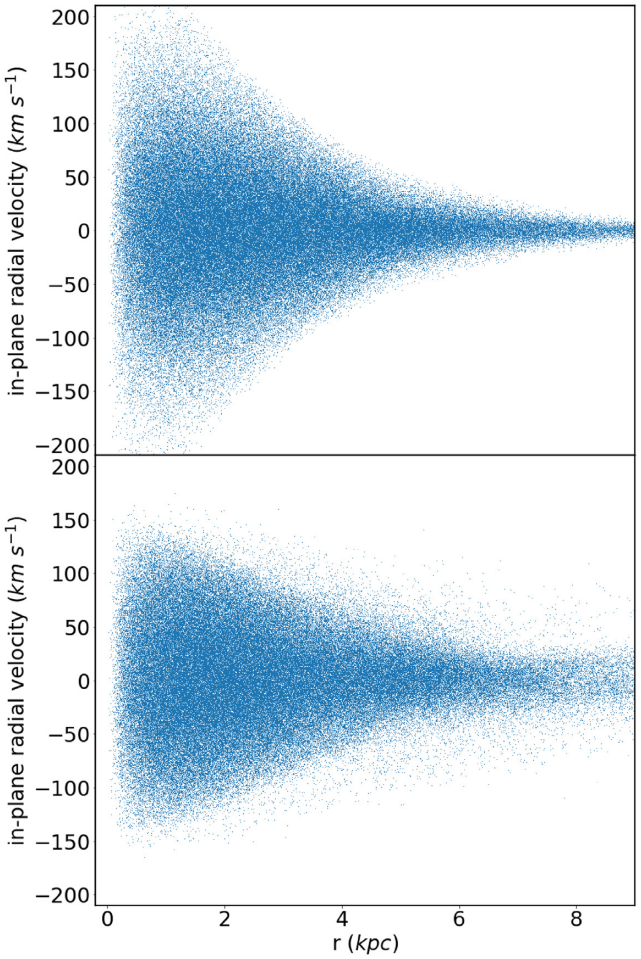

Figure 9. The radial profile of the initial/final (top/bottom panel) state of LMC–SMC interaction simulation (see Guglielmo, Lewis & Bland-Hawthorn 2014). The LMC–SMC interaction increases the dispersion and this effect is obvious at the outskirt of the LMC.

Zivick et al. 2019, etc). Joshi & Panchal (2019) found a common enhancement of the Cepheid population in both the LMC and SMC, suggesting an interaction ∼200 Myr ago between the Clouds. Schmidt et al. (2018) found the stars in the Magellanic Bridge are moving towards the LMC, supporting the idea that they, or the gas from which they formed, has been stripped from the SMC due to dynamical interactions. Finally, Olsen et al. (2011) suggested that a proportion of the carbon-rich AGB stars in the LMC may have come from the SMC. If this is correct then it is possible that there may be a non-disc, e.g. stripped SMC, component in our sample, potentially explaining in some part the observed spatial and kinematic offsets identified previously and inflating the observed dispersion.

We illustrate the effect of LMC–SMC interaction on the dispersion profile withe the 3 Gyr snapshot model from Guglielmo et al. (2014). The LMC and SMC have two close encounters during the integration. This simulation adopts an LMC mass of 1.9×10^{10} $M_\odot$ within 9 kpc, which is roughly comparable with, but somewhat smaller than, our result. Despite this mild discrepancy (see Section 3.2), the simulation should provide an indicative picture of the effect of LMC–SMC interactions.

Fig. 9 shows the initial and final state of the radial velocity profiles. The interaction between the LMC and SMC clearly increases the dispersion, which is more apparent in the outskirts of LMC. For example, at 5 kpc, the initial state has a tangential velocity dispersion of ~ 23.7 km s^{-1}, which increases to ~ 33.3 km s^{-1} at the final state. Simulations of an isolated LMC do not reproduce the observed dispersion, suggesting that this is not due to the natural evolution of the LMC. However, the LMC–SMC interaction model cannot fully reproduce the radial velocity profile (cf. Fig. 8), suggesting the current profile cannot be simply explained by LMC–SMC interactions alone. An alternative explanation is presented in Armstrong & Bekki (2018), based on the results in Olsen et al. (2011), the authors discussed the possibility that a third dwarf galaxy merging with LMC might have caused an increase in the velocity dispersion. However, this remains an open question.

3.4 Multi-population analysis

So far we have presented an analysis based on Carbon Stars from which we estimated the dynamical properties and the mass of the LMC. As previously described, we also identified two additional sets of stars: upper MS, and RGB stars (see Fig. 1). The dynamical

Downloaded from https://academic.oup.com/mnras/article/492/1/782/5674120 by guest on 22 May 2024

properties of these stars could potentially be different from those of the Carbon Stars since they trace populations of different ages and, therefore, have likely experienced different evolutionary histories. For example, we see that the bar clearly stands out with higher proper motion in the RGB sample but not in the Carbon Star sample. Furthermore, the upper MS stars formed only relatively recently and may therefore still retain a signature of their formation conditions rather than being fully mixed with older populations.

To characterize the dynamical properties of each population, we apply the same algorithm to the young MS and RGB stars as we do for the Carbon Star population. However, since there are more contaminants in the RGB and MS samples compared to the Carbon Stars, we exclude outliers by adding selection constraints on the proper motions: $1 < \mathrm{PM_{RA}} < 2.5$ mas yr^{-1} and $-1 < \mathrm{PM_{Dec.}} < 1.5$ mas yr^{-1}. Table 2 summarizes the best-fitting parameters for each population, with Figs B1 and B2 showing the corresponding parameter distributions for the RGB and MS stars. Our results suggest that the inferred bulk proper motions and the estimated circular velocities for the three populations roughly agree with each other.

The inferred inclination angles are relatively similar for all three populations; however the PA for the young MS stars is significantly different to that for the RGB and Carbon stars. Interestingly, this inclination is in good agreement with the inclination estimation from Red Clump [141.5 ± 4.5 from Subramanian & Subramaniam (2013) and 149.23 ± 8.35 from Choi et al. (2018)], RR Lyrae [150.76 ± 0.07 from Inno et al. (2016)], and especially young stars [147.4 ± 10 from van der Marel & Kallivayalil (2014)]. In addition, the rotation profile parameters ω and r_0 for Carbon Stars and RGB stars agree quite closely, but are rather different to those for the young MS stars, indicating the dynamics of young MS stars in the central regions of the LMC are indeed different to those for older stars.

The most striking difference between the young and old populations is in the inferred dynamical centres. The best-fitting dynamical centre for the young MS stars is $\sim 1^\circ$ away from the dynamical centre for the Carbon Stars and 0.7° away from the dynamical centre for the RGB stars, while the centres for the latter two population are very close to each other. In Fig. 10, we show the best-fitting dynamical centres for the three populations, compared to the photometric centre (van der Marel 2001) and the HI dynamical centre (Luks & Rohlfs 1992). The centre for the young MS stars is close to the photometric centre (0.1°), which is at the centre of the bar, and 1.19° away from the HI dynamical centre. Given the sample size of 3000 stars, tests using mock data indicate that our measurements are robust to within $\approx 0.2^\circ$, which agrees with the fitting results from Carbon Stars; moreover, since we apply the same algorithm to each stellar population, model-dependence cannot be the cause of the observed offsets.

The difference between the dynamical centres for the young stars and the HI gas out of which they presumably formed, is intriguing. One possibility is that the most recent LMC–SMC interaction, if it occurred after the majority of the young stars had formed (i.e. within the last $\sim$100–200 Myr) could have substantially perturbed the HI relative to the stars. It is also plausible that if the formation of the young stars was in fact triggered by an LMC–SMC interaction, that this star formation may not have been uniform within the HI, leading to an apparent discrepancy in their dynamical centres. A final possibility relates to additional forces felt by the gas compared to the stars, as a consequence of ram pressure due to the Milky Way's hot corona. For example, Belokurov et al. (2017) showed that RR Lyrae stars and the HI gas in the Magellanic Bridge – although both ostensibly stripped from the SMC – possess quite different spatial distributions, an observation they attribute to the effects of the Milky Way's corona. That the inferred bulk proper motion of the LMC is largely towards the east, whereas the dynamical centre of the HI gas sits to the west of that for the young stars, is consistent with this interpretation.

4 CONCLUSIONS

In this work, we select 3578 Carbon Stars candidates from SkyMapperDR1.1, including parallax information from *Gaia* DR2 to provide additional robustness; these Carbon Stars have very red $g - r$ colours, which are easily isolated using the $g - r$ versus g CMD. In addition, we also consider young MS and RGB stellar samples. From a comparison with a map of RGB stars, we note that the Carbon Star candidates are more likely located in the LMC disc, not showing the prominent bar features seen in the RGBs.

By assuming the stars are located and move in the disc, we construct a rotating planar model of the LMC and find the best-fitting geometric and kinematic parameters for the Carbon Star sample. The inferred properties of the LMC are in reasonable agreement with previous measurements (e.g. van der Marel et al. 2002; Olsen et al. 2011; Kallivayalil et al. 2013). In addition, we find a significant offset between the centre of the Carbon Star sample and both the HI dynamical centre and the photometric centre of the LMC, a signature that could result from the ongoing LMC–SMC interaction.

We applied the same fitting algorithm to the RGB stars and young MS stellar samples. The PA for the young stars is significantly different to the results from old stars, suggesting that they are drawn from different distributions. The dynamical centre for the RGB stars is close to the Carbon Star centre, and hence exhibits the same offset from the photometric centre. However, the dynamical centre for the young MS stars is close to the photometric centre and is significantly offset from the old populations, indicating that the young stars have different dynamical properties. We speculate the observed offset – between the dynamical centre for the young stars and that for the HI gas out of which they presumably formed – may reflect the effects of a possible LMC–SMC interaction in the period since the young stars formed, and/or the additional forces felt by the gas compared to the stars, due to ram pressure from the Milky Way's hot corona.

Using a simulation of the LMC–SMC interaction, we illustrate that this can increase the observed velocity dispersion, but further interactions, possibly with a third dwarf galaxy, may be needed to fully account for the observations. Our model contains a constant dispersion and it is weighted by the data. Compared to Vasiliev (2018), it hence overestimates the dispersion in the velocity profiles at large radii.

From the tangential velocity profile and its dispersion, we measure the circular velocity to be $V_{\mathrm{circ}} \sim 123.6 \pm 1.9$ km s^{-1} at 7 kpc, implying an LMC mass within 7 kpc of $(2.5 \pm 0.1) \times 10^{10}\,\mathrm{M}_\odot$. From this, we estimate the total LMC mass within 30 kpc to be $(1.06 \pm 0.32) \times 10^{10}$ $\mathrm{M}_\odot$ under the assumption of a constant circular velocity to the tidal radius. The radial dispersion significantly contributes to the mass estimation via the *asymmetric drift* correction. Since we adopt a model with a constant dispersion, which may consequently overestimate the dispersion at larger radii, the mass we estimate here plausibly represents an upper limit for the LMC mass within 30 kpc, and we note that a better mass estimation would require an accurate tidal radius estimation. The mass determined in this present study, whilst significantly smaller than some of very massive LMC models considered in

Downloaded from https://academic.oup.com/mnras/article/492/1/782/5674120 by guest on 22 May 2024

Table 2. This table summaries the best-fitting parameters for the Carbon Stars, RGB stars, and Young MS stars. Note that here we assume the same κ for the *asymmetric drift* correction when calculating the circular velocity (see Section 3.2).

Population	α_0 (°)	δ_0 (°)	μ_α (mas yr^{-1})	μ_δ (mas yr^{-1})	PA (°)	i (°)
Carbon Stars	80.90 ± 0.29	−68.74 ± 0.12	1.878 ± 0.007	0.293 ± 0.018	135.6 ± 3.3	25.6 ± 1.1
RGB Stars	81.23 ± 0.02	−69.00 ± 0.01	1.824 ± 0.001	0.355 ± 0.002	134.1 ± 0.4	26.1 ± 0.14
Young MS stars	80.98 ± 0.08	−69.69 ± 0.02	1.860 ± 0.002	0.359 ± 0.005	152.0 ± 1.0	29.4 ± 0.45
Population	ω (km s^{-1} kpc^{-1})	r_0 (kpc)	σ_r (mas yr^{-1})	σ_θ (mas yr^{-1})	$V_{\rm Circ}$ (km s^{-1})	
Carbon Stars	24.6 ± 0.6	3.39 ± 0.12	0.157 ± 0.003	0.158 ± 0.003	123.6 ± 1.9	
RGB Stars	23.3 ± 0.1	3.14 ± 0.02	0.183 ± 0.001	0.170 ± 0.001	128.9 ± 0.3	
Young MS stars	38.5 ± 0.6	1.84 ± 0.03	0.174 ± 0.001	0.156 ± 0.001	122.9 ± 0.7	

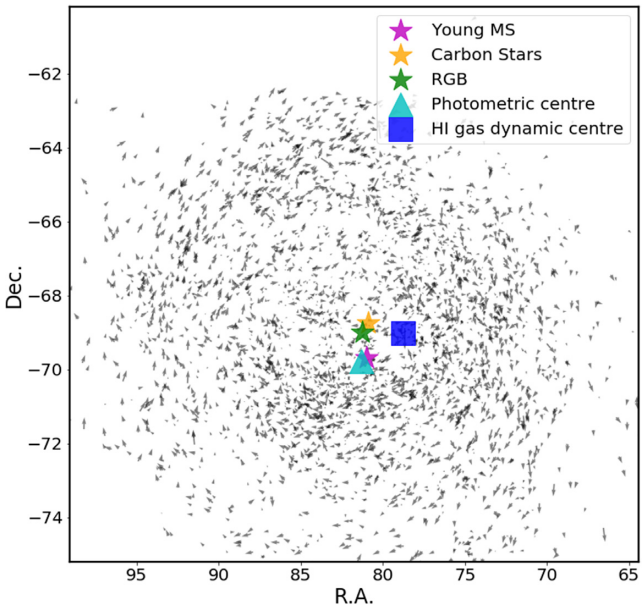

Figure 10. The best-fitting centre for young MS stars, Carbon Stars, and RGB stars, compared to the photometric centre (van der Marel 2001) and photometric centre (Luks & Rohlfs 1992). On the background is the internal proper motion map of Carbon Stars. The dynamical centre of the young MS stars is close to the photometric centre. The dynamical centre of the RGB stars and Carbon Stars are close to each other, but roughly 1° away from the young MS star and the photometric centre.

the literature, is consistent with the mass estimation from tidal-interaction and perturbation considerations (e.g. Erkal et al. 2019; Erkal & Belokurov 2019).

ACKNOWLEDGEMENTS

ZW gratefully acknowledges financial support through a the Dean's International Postgraduate Research Scholarship from the Physics School of the University of Sydney. DM holds an Australian Research Council (ARC) Future Fellowship (FT160100206). We thank the anonymous reviewer for their constructive suggestions.

The national facility capability for SkyMapper has been funded through ARC LIEF grant LE130100104 from the Australian Research Council, awarded to the University of Sydney, the Australian National University, Swinburne University of Technology, the University of Queensland, the University of Western Australia, the University of Melbourne, Curtin University of Technology, Monash University and the Australian Astronomical Observatory. SkyMapper is owned and operated by The Australian National University's Research School of Astronomy and Astrophysics. The survey data were processed and provided by the SkyMapper Team at ANU. The SkyMapper node of the All-Sky Virtual Observatory (ASVO) is hosted at the National Computational Infrastructure (NCI). Development and support the SkyMapper node of the ASVO has been funded in part by Astronomy Australia Limited (AAL) and the Australian Government through the Commonwealth's Education Investment Fund (EIF) and National Collaborative Research Infrastructure Strategy (NCRIS), particularly the National eResearch Collaboration Tools and Resources (NeCTAR) and the Australian National Data Service Projects (ANDS).

This work has made use of data from the European Space Agency (ESA) mission *Gaia* (https://www.cosmos.esa.int/gaia), processed by the *Gaia* Data Processing and Analysis Consortium (DPAC, https://www.cosmos.esa.int/web/gaia/dpac/consortium). Funding for the DPAC has been provided by national institutions, in particular the institutions participating in the Gaia Multilateral Agreement.

REFERENCES

Armstrong B., Bekki K., 2018, MNRAS, 480, L141
Belcheva M. K., Livanou E., Kontizas M., Nikolov G. B., Kontizas E., 2011, A&A, 527, A31
Belokurov V., Erkal D., Deason A. J., Koposov S. E., De Angeli F., Evans D. W., Fraternali F., Mackey D., 2017, MNRAS, 466, 4711
Belokurov V. A., Erkal D., 2019, MNRAS, 482, L9
Besla G., Kallivayalil N., Hernquist L., Robertson B., Cox T. J., van der Marel R. P., Alcock C., 2007, ApJ, 668, 949
Besla G., Kallivayalil N., Hernquist L., van der Marel R. P., Cox T. J., Kereš D., 2010, ApJ, 721, L97
Besla G., Kallivayalil N., Hernquist L., van der Marel R. P., Cox T. J., Kereš D., 2012, MNRAS, 421, 2109
Besla G., Martínez-Delgado D., van der Marel R. P., Beletsky Y., Seibert M., Schlafly E. F., Grebel E. K., Neyer F., 2016, ApJ, 825, 20
Bessell M., Bloxham G., Schmidt B., Keller S., Tisserand P., Francis P., 2011, PASP, 123, 789
Brüns C. et al., 2005, A&A, 432, 45
Carrera R., Conn B. C., Noël N. E. D., Read J. I., López Sánchez Á. R., 2017, MNRAS, 471, 4571
Cautun M., Deason A. J., Frenk C. S., McAlpine S., 2019, MNRAS, 483, 2185
Chen Y.-P., Trager S. C., Peletier R. F., Lançon A., Vazdekis A., Prugniel P., Silva D. R., Gonneau A., 2014, A&A, 565, A117
Choi Y. et al., 2018, ApJ, 866, 90
Cioni M. R. L., Habing H. J., Israel F. P., 2000, A&A, 358, L9
de Grijs R., Wicker J. E., Bono G., 2014, AJ, 147, 122
Deb S., Singh H. P., 2014, MNRAS, 438, 2440

Downloaded from https://academic.oup.com/mnras/article/492/1/782/5674120 by guest on 22 May 2024

Dehnen W., Binney J. J., 1998, MNRAS, 298, 387
Erkal D., Belokurov V. A., 2019, preprint (arXiv:1907.09484)
Erkal D. et al., 2019, MNRAS, 487, 2685
Foreman-Mackey D., Hogg D. W., Lang D., Goodman J., 2013, PASP, 125, 306
Foreman-Mackey D. et al., 2016, corner.py: corner.py v2.0.0. Available at: https://doi.org/10.5281/zenodo.53155 (accessed October 04, 2019)
Freeman K. C., Illingworth G., Oemler A. J., 1983, ApJ, 272, 488
Gaia Collaboration et al., 2016, A&A, 595, A1
Gaia Collaboration et al., 2018, A&A, 616, A1
Garavito-Camargo N., Besla G., Laporte C. F. P., Johnston K. V., Gómez F. A., Watkins L. L., 2019, ApJ, 884, 51
Graff D. S., Gould A. P., Suntezeff N. B., Schommer R. A., Hardy E., 2000, ApJ, 540, 211
Guglielmo M., Lewis G. F., Bland-Hawthorn J., 2014, MNRAS, 444, 1759
Hardy E., Alves D. R., Graff D. S., Suntzeff N. B., Schommer R. A., 2001, Ap&SS, 277, 471
Harris J., Zaritsky D., 2009, AJ, 138, 1243
Haschke R., Grebel E. K., Duffau S., 2012, AJ, 144, 106
Helmi A. et al., 2018, A&A, 616, A12
Inno L. et al., 2016, ApJ, 832, 176
Jacyszyn-Dobrzeniecka A. M. et al., 2016, Acta Astron., 66, 149
Joshi Y. C., Panchal A., 2019, A&A, 628, A51
Kallivayalil N., Van Der Marel R. P., Besla G., Anderson J., Alcock C., 2013, ApJ, 764, 161
Kim S., Staveley-Smith L., Dopita M. A., Freeman K. C., Sault R. J., Kesteven M. J., McConnell D., 1998, ApJ, 503, 674
Kontizas E., Dapergolas A., Morgan D. H., Kontizas M., 2001, A&A, 369, 932
Kunkel W. E., Irwin M. J., Demers S., 1997, A&AS, 122, 463
Luks T., Rohlfs K., 1992, A&A, 263, 41
Mackey D., Koposov S., Da Costa G., Belokurov V., Erkal D., Kuzma P., 2018, ApJ, 858, L21
Mackey A. D., Koposov S. E., Da Costa G. S., Belokurov V., Erkal D., Fraternali F., McClure-Griffiths N. M., Fraser M., 2017, MNRAS, 472, 2975
Martinez-Delgado D. et al., 2019, preprint (arXiv:1907.02264)
McClure-Griffiths N. M. et al., 2018, Nat. Astron., 2, 901
McConnachie A. W., 2012, AJ, 144, 4
Meatheringham S. J., Dopita M. A., Ford H. C., Webster B. L., 1988, ApJ, 327, 651
Moretti M. I. et al., 2014, MNRAS, 437, 2702
Navarrete C. et al., 2019, MNRAS, 483, 4160
Nidever D. L. et al., 2019, ApJ, 874, 118
Nikolaev S., Weinberg M. D., 2000, ApJ, 542, 804
Noël N. E. D., Conn B. C., Carrera R., Read J. I., Rix H.-W., Dolphin A., 2013, ApJ, 768, 109
Olsen K. A. G., Salyk C., 2002, AJ, 124, 2045
Olsen K. A. G., Zaritsky D., Blum R. D., Boyer M. L., Gordon K. D., 2011, ApJ, 737, 29
Peñarrubia J., Gómez F. A., Besla G., Erkal D., Ma Y.-Z., 2016, MNRAS, 456, L54
Schlafly E. F., Finkbeiner D. P., 2011, ApJ, 737, 103
Schlegel D. J., Finkbeiner D. P., Davis M., 1998, ApJ, 500, 525
Schmidt T., Cioni M.-R., Niederhofer F., Diaz J., Matijevic G., 2018, in Proc. IAU Symp. 344, Dwarf Galaxies: From the Deep Universe to the Present, Kluwer, Dordrecht, p. 130
Shao S., Cautun M., Deason A. J., Frenk C. S., Theuns T., 2018, MNRAS, 479, 284
Stanimirović S., Staveley-Smith L., Jones P. A., 2004, ApJ, 604, 176
Staveley-Smith L., Kim S., Calabretta M. R., Haynes R. F., Kesteven M. J., 2003, MNRAS, 339, 87
Subramanian S., Subramaniam A., 2013, A&A, 552, A144
Subramanian S., Subramaniam A., 2015, A&A, 573, A135
Tepper-García T., Bland-Hawthorn J., Pawlowski M. S., Fritz T. K., 2019, MNRAS, 488, 918
van der Marel R. P., 2001, AJ, 122, 1827
van der Marel R. P., Kallivayalil N., 2014, ApJ, 781, 121
van der Marel R. P., Alves D. R., Hardy E., Suntzeff N. B., 2002, AJ, 124, 2639
Vasiliev E., 2018, MNRAS, 481, L100
Wolf C. et al., 2018, PASA, 35, e010
Zaritsky D., Harris J., Grebel E. K., Thompson I. B., 2000, ApJ, 534, L53
Zivick P. et al., 2019, ApJ, 874, 78

APPENDIX A: LMC MODEL

As noted in Section 3, we assume the stars in the LMC disc plane are on circular orbits so:

$$V_\phi = \omega\, r, \ \text{for}\ r < r_0$$
$$V_\phi = \omega\, r_0, \ \text{for}\ r \geq r_0$$
$$\boldsymbol{V} = (v_\mathrm{x}, v_\mathrm{y}, v_\mathrm{z}) = (-V_\phi \sin(\phi), V_\phi \cos(\phi), 0) + \boldsymbol{V_{\mathrm{bulk}}}$$

Here, the r and ϕ will depend on the configuration of LMC and are functions of stars' sky position and V_{bulk} is the constant bulk motion. We then assume constant dispersion in both tangential and radial directions:

$$p(v_\mathrm{r}, v_\phi) = \frac{1}{2\pi\sigma_\mathrm{r}\sigma_\phi} \exp\left[-\left(\frac{(v_\phi - V_\phi(r))^2}{2\sigma_\phi^2} + \frac{{v_\mathrm{r}}^2}{2{\sigma_\mathrm{r}}^2}\right)\right]$$

Assume the configuration of LMC: position angle θ, inclination i and centre (α_0, δ_0), we derive the model prediction on the proper motion would be:

$$\boldsymbol{V}_{\mathrm{sky}} = \mathbb{R}_\mathrm{x}(i) \cdot \mathbb{R}_\mathrm{z}(\theta - \pi) \cdot \mathbb{R}_\mathrm{x}(\delta_0 - \frac{\pi}{2}) \cdot \mathbb{R}_\mathrm{z}(\alpha_0 - \frac{\pi}{2}) \cdot \boldsymbol{V}$$
$$\mu_\alpha = -V_{\mathrm{sky}}(x)\sin(\alpha) + V_{\mathrm{sky}}(y)\cos(\alpha)$$
$$\mu_\delta = V_{\mathrm{sky}}(z)\cos(\delta) - (V_{\mathrm{sky}}(x)\cos(\alpha) + V_{\mathrm{sky}}(y)\sin(\alpha))\sin(\delta)$$

Downloaded from https://academic.oup.com/mnras/article/492/1/782/5674120 by guest on 22 May 2024

This projection sets up a correlation between proper motion and in-plane velocity $v_{\rm phi}$, $v_{\rm rot}$:

$$
\begin{aligned}
\mu_\alpha &= P_1 v_\phi + P_2 v_{\rm r} + V\alpha_{\rm bulk}(\alpha,\delta)\\
\mu_\delta &= P_3 v_\phi + P_4 v_{\rm r} + V\delta_{\rm bulk}(\alpha,\delta)\\
P_1 &= \cos(i)\cos(\phi)(\cos(\alpha_0)(\sin(\delta_0)\cos(\theta)\sin(\alpha) - \sin(\theta)\cos(\alpha)) - \sin(\alpha_0)(\sin(\delta_0)\cos(\theta)\cos(\alpha)\\
&\quad + \sin(\theta)\sin(\alpha))) - \cos(\delta_0)\sin(i)\cos(\phi)\sin(\alpha-\alpha_0) - \sin(\phi)(\sin(\delta_0)\sin(\theta)\sin(\alpha)\cos(\alpha_0)\\
&\quad - \sin(\delta_0)\sin(\theta)\cos(\alpha)\sin(\alpha_0) + \cos(\theta)\cos(\alpha)\cos(\alpha_0) + \cos(\theta)\sin(\alpha)\sin(\alpha_0))\\
P_2 &= (\sin(\phi) + \cos(\phi))(\cos(i)(\cos(\alpha_0)(\sin(\delta_0)\cos(\theta)\sin(\alpha)\\
&\quad - \sin(\theta)\cos(\alpha)) - \sin(\alpha_0)(\sin(\delta_0)\cos(\theta)\cos(\alpha) + \sin(\theta)\sin(\alpha))) - \cos(\delta_0)\sin(i)\sin(\alpha-\alpha_0))\\
P_3 &= \cos(\phi)(\cos(\delta)(\cos(\delta_0)\cos(\theta)\cos(i) + \sin(\delta_0)\sin(i)) + \sin(\delta)(\cos(i)(\sin(\delta_0)\cos(\theta)\cos(\alpha)\cos(\alpha_0)\\
&\quad + \sin(\delta_0)\cos(\theta)\sin(\alpha)\sin(\alpha_0) + \sin(\theta)\sin(\alpha)\cos(\alpha_0) - \sin(\theta)\cos(\alpha)\sin(\alpha_0))\\
&\quad - \cos(\delta_0)\sin(i)\cos(\alpha-\alpha_0))) - \sin(\phi)(\sin(\theta)(\sin(\delta)\sin(\delta_0)\sin(\alpha)\sin(\alpha_0)\\
&\quad + \cos(\delta)\cos(\delta_0)) + \sin(\delta)\cos(\alpha_0)(\sin(\delta_0)\sin(\theta)\cos(\alpha) - \cos(\theta)\sin(\alpha)) + \sin(\delta)\cos(\theta)\cos(\alpha)\sin(\alpha_0))\\
P_4 &= \sin(\phi)(\cos(\delta)(\cos(\delta_0)\cos(\theta)\cos(i) + \sin(\delta_0)\sin(i)) + \sin(\delta)(\cos(i)(\sin(\delta_0)\cos(\theta)\cos(\alpha)\cos(\alpha_0)\\
&\quad + \sin(\delta_0)\cos(\theta)\sin(\alpha)\sin(\alpha_0) + \sin(\theta)\sin(\alpha)\cos(\alpha_0) - \sin(\theta)\cos(\alpha)\sin(\alpha_0))\\
&\quad - \cos(\delta_0)\sin(i)\cos(\alpha-\alpha_0))) + \cos(\phi)(\sin(\theta)(\sin(\delta)\sin(\delta_0)\sin(\alpha)\sin(\alpha_0)\\
&\quad + \cos(\delta)\cos(\delta_0)) + \sin(\delta)\cos(\alpha_0)(\sin(\delta_0)\sin(\theta)\cos(\alpha) - \cos(\theta)\sin(\alpha)) + \sin(\delta)\cos(\theta)\cos(\alpha)\sin(\alpha_0))
\end{aligned}
$$

And on the other hand, we have:

$$
\begin{aligned}
v_\phi &= A_1\mu_\alpha + A_2\mu_\delta\\
v_{\rm r} &= B_1\mu_\alpha + B_2\mu_\delta\\
A_1 &= \frac{-P_4}{P_2P_3 - P_1P_4},\ A_2 = \frac{P_2}{P_2P_3 - P_1P_4}\\
B_1 &= \frac{P_3}{P_2P_3 - P_1P_4},\ B_2 = \frac{-P_1}{P_2P_3 - P_1P_4}
\end{aligned}
$$

Since this is a linear transformation of a 2D Gaussian probability distribution, we expect the probability distribution in proper motion space is also a Gaussian distribution. The standard deviation and mean values are:

$$
\begin{aligned}
\sigma^2_{\alpha,\rm Model} &= P_1^2\sigma_\phi^2 + P_2^2\sigma_r^2\\
\sigma^2_{\delta,\rm Model} &= P_3^2\sigma_\phi^2 + P_4^2\sigma_r^2\\
\mu_{\alpha,\rm Model} &= P_1 V_\phi(r) + V\alpha_{\rm bulk}(\alpha,\delta)\\
\mu_{\delta,\rm Model} &= P_3 V_\phi(r) + V\alpha_{\rm bulk}(\alpha,\delta)
\end{aligned}
$$

We incorporate the data uncertainty as:

$$
\begin{aligned}
\sigma^2_\alpha &= \sigma^2_{\alpha,\rm Model} + \sigma^2_{\alpha,\rm Data}\\
\sigma^2_\delta &= \sigma^2_{\delta,\rm Model} + \sigma^2_{\delta,\rm Data}
\end{aligned}
$$

Then, the correlation is

$$
\rho = \frac{A_1B_1\sigma_\phi^2 + A_2B_2\sigma_{\rm r}^2}{\sigma_\alpha\sigma_\delta}
$$

The probability distribution in proper motion space:

$$
p(\mu_\alpha,\mu_\delta) = \frac{1}{2\pi\sigma_\alpha\sigma_\delta\sqrt{1-\rho^2}}\exp\left[-\frac{1}{(1-\rho^2)}\left(\frac{(\mu_\alpha-\mu_{\alpha,\rm Model})^2}{2\sigma_\alpha^2} + \frac{(\mu_\delta-\mu_{\delta,\rm Model})^2}{2\sigma_\delta^2} - \rho\frac{(\mu_\alpha-\mu_{\alpha,\rm Model})(\mu_\delta-\mu_{\delta,\rm Model})}{\sigma_\alpha\sigma_\delta}\right)\right]
$$

Downloaded from https://academic.oup.com/mnras/article/492/1/782/5674120 by guest on 22 May 2024

APPENDIX B: MCMC SAMPLING RESULTS FOR RGB AND YOUNG STARS

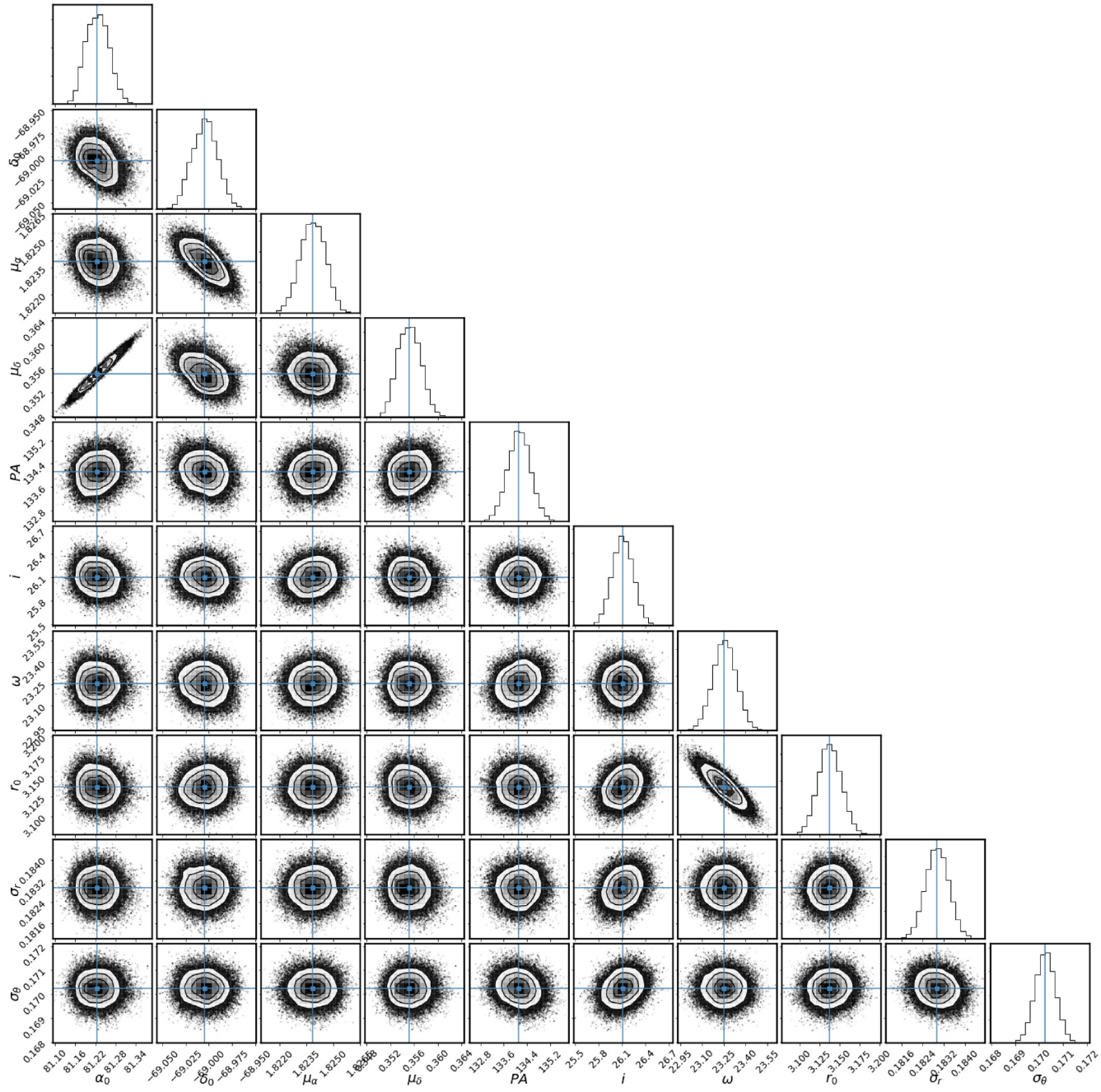

Figure B1. Corner plot summary of the MCMC sampling result for the RGB stars. The sample size for this population is much larger than for the Carbon Stars, but the degree of contamination is also greater.

Downloaded from https://academic.oup.com/mnras/article/492/1/782/5674120 by guest on 22 May 2024

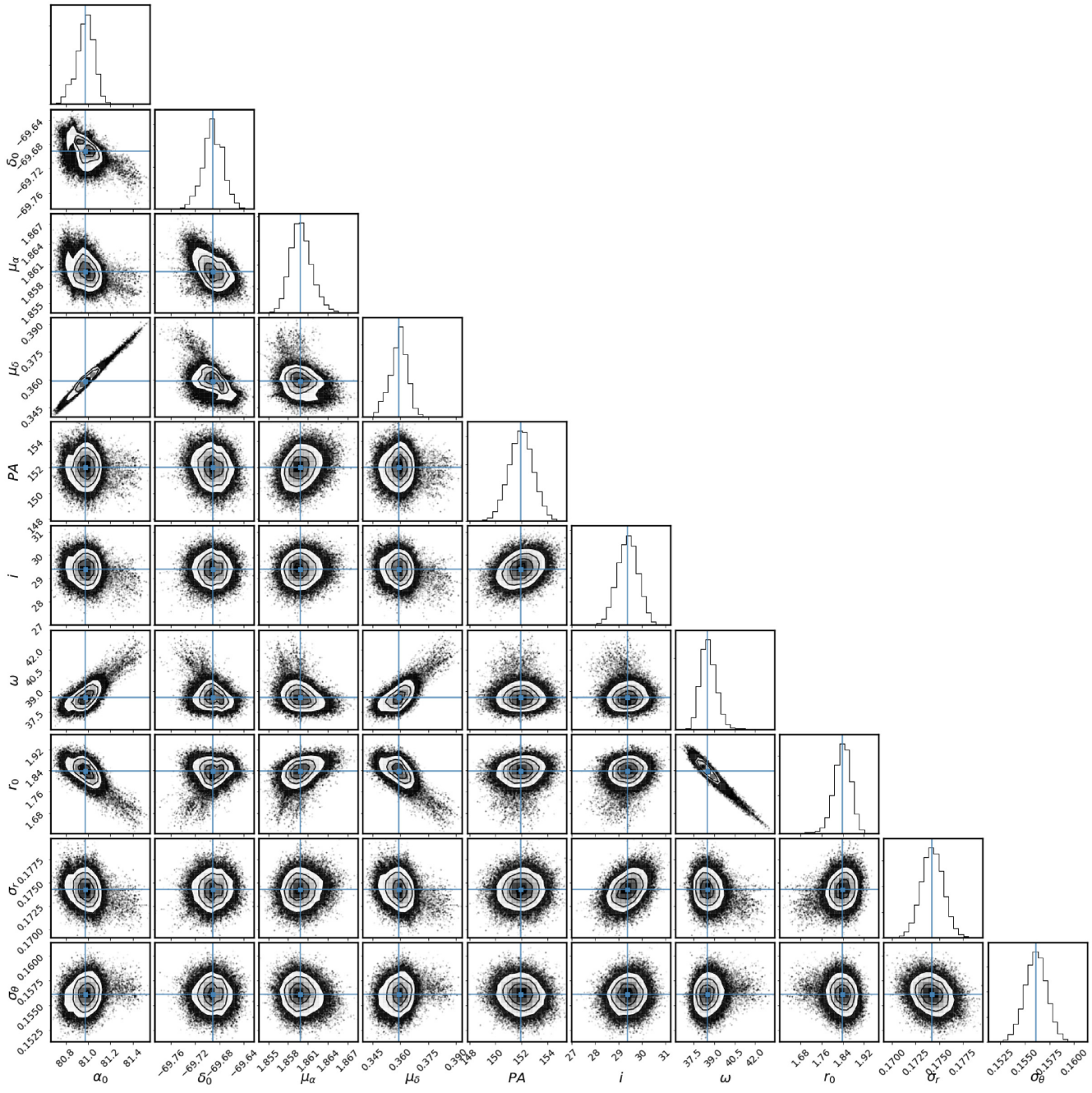

Figure B2. Corner plot summary of the MCMC sampling result for the young MS stars. There are similar correlations evident as in Fig. 6.

This paper has been typeset from a TEX/LATEX file prepared by the author.

Downloaded from https://academic.oup.com/mnras/article/492/1/782/5674120 by guest on 22 May 2024